Applied Surface Science 696 (2025) 162959

Contents lists available at ScienceDirect

Applied Surface Science

journal homepage: www.elsevier.com/locate/apsusc

Full Length Article

Dual-sensitized hollow SnO_2 nanospheres with rGO and Pd for highly sensitive detection of acetone in exhaled breath

Arunkumar Shanmugasundaram [a,b,1], Kun Woo Baek [c,1], Changung Paeng [d,1], Longlong Li [a], Goeun Cha [e], Jonghyeon Woo [g], Dong-Su Kim [a], Changyong Yim [d,e,f], Jongsung Park [g], Jung Sang Cho [c,h,i,*], Dong-Weon Lee [a,b,j,**]

[a] MEMS and Nanotechnology Laboratory, School of Mechanical Engineering, Chonnam National University (CNU), Gwangju 61186, Republic of Korea
[b] Advanced Medical Device Research Center for Cardiovascular Disease, Chonnam National University (CNU), Gwangju 61186, Republic of Korea
[c] Department of Engineering Chemistry, Chungbuk National University (CNU), Chungbuk 361-763, Republic of Korea
[d] Department of Energy Materials & Chemical Engineering, Kyungpook National University (KNU), 2559 Gyeongsang-daero, Sangju-si, Gyeongsangbuk-do 37224, Republic of Korea
[e] School of Advanced Science and Technology Convergence, Kyungpook National University (KNU), 2559 Gyeongsang-daero, Sangju-si, Gyeongsangbuk-do 37224, Republic of Korea
[f] Department of Energy Chemical Engineering, Kyungpook National University (KNU), 2559 Gyeongsang-daero, Sangju-si, Gyeongsangbuk-do 37224, Republic of Korea
[g] Department of Precision Mechanical Engineering, Kyungpook National University (KNU), 2559 Gyeongsang-daero, Sangju-si, Gyeongsangbuk-do 37224, Republic of Korea
[h] Biomedical Research Institute, Chungbuk National University Hospital, Chungbuk 28644, Republic of Korea
[i] Advanced Energy Research Institute, Chungbuk National University, Cheongju, Chungbuk 28644, Republic of Korea
[j] Center for Next-Generation Sensor Research and Development, Chonnam National University (CNU), Gwangju 61186, Republic of Korea

ARTICLE INFO

Keywords:
Reduced graphene oxide
Pd catalysts
SnO_2 hollow spheres
Acetone sensor
Exhaled breath analysis

ABSTRACT

Detecting acetone in human breath is crucial for the early diagnosis of metabolic disorders such as diabetes. Metal oxide semiconductor (MOS) based acetone breath sensors have received considerable attention due to their compactness and noninvasive nature. However, their limited sensitivity and interference from humidity present challenges in selectively detecting acetone. Herein, we propose sensors based on tin oxide hollow spheres dual-sensitized with reduced graphene oxide and ultrafine palladium nanoparticles (rGO-Sn-HS-Pd) for enhanced and selective detection of acetone. The Sn-HS are synthesized using a spray pyrolysis technique, followed by a hydrothermal process to achieve the rGO-Pd-NPs dual-sensitized SnO_2 hollow spheres. The rGO-Sn-HS-Pd sensor demonstrate high sensitivity to acetone, exceptional selectivity, and fast response/ recovery. Furthermore, by utilizing a linear fitting approach on the experimental response data for acetone concentrations, it is estimated that the rGO_2-Sn-HS-Pd_2 sensor can detect acetone as low as 220 ppb. The optimized rGO_2-Sn-HS-Pd_2 sensor demonstrates performance that is 7.35, 5.38, 3.87, 4.57, 1.27, and 1.15 times higher compared to the bare Sn-HS, rGO_1-Sn-HS, rGO_2-Sn-HS, rGO_3-Sn-HS, rGO_2-Sn-HS-Pd_1, and rGO_2-Sn-HS-Pd_3 sensors. Sensor arrays incorporating rGO_2-Sn-HS-Pd_2 can distinguish breath patterns between healthy and simulated diabetic breath through principal component analysis, presenting a promising avenue for noninvasive diabetes screening and monitoring.

1. Introduction

Detecting acetone in exhaled breath is crucial for diagnosing metabolic and systemic diseases, notably diabetes. Healthy individuals typically exhibit 0.3 to 0.9 ppm breath acetone levels, while significantly higher levels indicate pathological conditions [1–4]. Traditional analysis methods like proton-transfer-reaction and secondary ion mass spectrometry are precise but unsuitable for point-of-care use due to their

* Corresponding author at: Department of Engineering Chemistry, Chungbuk National University (CNU), Chungbuk 361-763, Republic of Korea.
** Corresponding author at: MEMS and Nanotechnology Laboratory, School of Mechanical Engineering, Chonnam National University (CNU), Gwangju, 61186, Republic of Korea.
E-mail addresses: jscho@cbnu.ac.kr (J.S. Cho), mems@jnu.ac.kr (D.-W. Lee).
[1] Authors are equally contributed.

https://doi.org/10.1016/j.apsusc.2025.162959
Received 25 December 2024; Received in revised form 3 March 2025; Accepted 11 March 2025
Available online 13 March 2025

cost, size, complexity, and specialized operating requirements [5,6]. This highlights the urgent need for compact, affordable, and user-friendly breath analysis devices [7]. Further, given acetone's widespread industrial use and potential long-term health risks (including liver, kidney, and pancreas damage), sensitive and selective acetone sensors are essential for both disease diagnosis and industrial safety [8].

The MOS gas sensors are favored for acetone detection due to their rapid response, high sensitivity, affordability, and potential for miniaturization [9–12]. Among various metal oxides, SnO_2 is widely recognized for its excellent physicochemical properties [13,14]. Research has shown that hierarchical mesoporous SnO_2 nanostructures are effective acetone detectors due to their large surface area, providing more sites for gas interaction [15–19]. However, their high operating temperatures can compromise selectivity and sensitivity due to nonspecific interactions with interfering gases. To enhance sensitivity and selectivity, SnO_2-based hybrid nanocomposites and heterostructures have been explored. For example, Wang et al. proposed hierarchical TiO_2-SnO_2-TiO_2 nanofibers for acetone detection, demonstrating sensitivity to 1 ppm at 280 °C with rapid response and recovery times. Similarly, Li et al. developed a Nb_2O_5@SnO_2 hybrid with ppb-level sensitivity and high selectivity at 250 °C. Other notable structures have shown promising acetone sensing performance [20–25]. In recent years, substantial progress has been made in the development of high-performance metal oxide-based acetone gas sensors, with several studies demonstrating remarkable sensitivity and selectivity under simulated breath analysis conditions [24,25]. For instance, Zhou et al. reported an ultrasensitive acetone sensor utilizing $ZnFe_3O_4$ nanostructures, which exhibited excellent performance for diabetes diagnosis due to its high response, selectivity, and stability under breath-like conditions [24]. Similarly, Ji et al. developed a Sn and Ni co-doped Co_3O_4 sensor that effectively detected acetone in exhaled breath, benefiting from synergistic effects that enhanced its sensing performance, including improved catalytic activity, charge transfer efficiency, and selectivity toward acetone over interfering gases [25]. However, most of reported acetone sensors were investigated under conditions of dry environment or low humidity atmosphere, failing to replicate the high moisture content characteristic of human exhalation, where humidity levels can markedly affect sensor sensitivity to specific analytes [26–30]. The dual objectives of enhanced sensitivity and selectivity present significant challenges in the development of breath analyzers aimed at the accurate diagnosis of diseases. Given that exhaled breath typically exhibits humidity levels ranging from 85 to 95 % RH, moisture becomes a predominant interfering agent, substantially influencing the performance of gas sensors [31–33]. In response to the challenge of identifying specific biomarkers within the humid environment of exhaled breath, a variety of approaches have been proposed [34–37]. Among these, the application of noble metal catalysts to MOS gas sensors has been thoroughly researched, showing considerable promise in improving both the selectivity and sensitivity of these detection systems [38–41].

In this work, we propose the dual sensitization of rGO and Pd NPs on SnO_2 hollow spheres for the selective and sensitive detection of acetone in exhaled breath. The hierarchical mesoporous SnO_2 hollow spheres were synthesized via the spray pyrolysis technique. To optimize the sensing performance of the sensor and improve its sensitivity and selectivity, the hollow spheres were functionalized with rGO and Pd nanoparticles. The fabricated sensors, based on rGO$_2$-Sn-HS-Pd$_2$, significantly enhance the sensor's performance towards acetone, maintaining high sensitivity even under elevated humidity conditions (85 % RH). The enhanced gas sensing response of the proposed sensor, based on rGO-Sn-HS-Pd, is attributed to the sensitization effect, which is due to the increased surface area from the large specific surface area of the rGO nanosheets and to the enhanced electron transport in the graphene–SnO_2 hollow spheres nanocomposite structures, as well as the improved catalytic activity of ultrafine Pd NPs. Additionally, we have explored the promising application of the catalyst-loaded, porous rGO-Sn-HS-Pd platforms for non-invasive breath sensors.

2. Experimental section

2.1. Preparation of porous SnO_2 hollow spheres (Sn-HS)

The porous SnO_2 nanospheres were synthesized by a one-pot spray pyrolysis technique (**Fig. S1**). The spray solution was prepared by adding 0.1 M of $SnCl_4{\cdot}5H_2O$ (SAMCHUN, Mw = 350.58, 98.0 %) and 2.0 g of PVP (DAEJUNG, Mw = 40,000) in 100 mL of distilled water. The solution was stirred for 1 h until a homogeneous solution was achieved. Next, polystyrene (PS) nanobead suspension (100 mL, φ = 100 nm) was added to the above solution and stirred vigorously. The size-controlled PS nanobeads, employed as pore generator, were prepared using the polymerization method previously reported elsewhere [42]. Afterwards, the final solution was transferred to a 1.7 MHz ultrasonic nebulizer as a droplet generator consisting of six vibrators. The droplets generated through an ultrasonic nebulizer were fed into a vertical quartz reactor (length = 1200 mm, diameter = 50 mm) with the reactor temperature set at 700 °C using an air carrier gas (10 L/min). The powder collected after spray pyrolysis was successfully synthesized porous pure SnO_2 nanospheres.

2.2. Preparation of rGO-SnO_2 hollow spheres (rGO-Sn-HS)

Graphene oxide (GO) was synthesized from natural graphite via a modified Hummer's method, detailed in Supplementary Information [43]. Initially, GO was ultrasonically dispersed in DI water to form a 2 mg/mL solution. Subsequently, 6 mL of this GO solution was further dispersed in a 36 mL mixture of DI water and ethanol (1:1 ratio). Then, 180 mg of pre-prepared Sn-HS nanospheres were added and ultrasonically dispersed for 15 min. The mixture was transferred to a Teflon-lined autoclave and heated at 120 °C for 12 h. Afterward, the autoclave was cooled to room temperature. The resultant rGO$_1$-Sn-HS was purified through multiple washes with DI water and ethanol, followed by centrifugation. Finally, the product was dried at 75 °C for 24 h. Similar protocols were followed to prepare the rGO$_2$-Sn-HS and rGO$_3$-Sn-HS hybrid nanocomposites, except for varying the GO weight ratio in the reaction mixture. The rGO weight ratios in rGO$_1$-Sn-HS, rGO$_2$-Sn-HS, and rGO$_3$-Sn-HS were theoretically set at 2, 4, and 6 wt%, respectively.

2.3. Preparation of rGO-SnO_2-Pd hollow spheres (rGO-Sn-HS-Pd)

Initially, 9 mL of 1 mM $PdCl_2$ and 100 mg of polyvinylpyrrolidone (PVP) [$PdCl_2$/PVP ratio = 1:5 M] were stirred for 2 h at 25 °C. Additionally, 6 mL of GO solution was mixed with 27 mL of DI water and ethanol (1:1 ratio). Then, 180 mg of Sn-HS nanospheres were added and ultrasonically dispersed for 15 min. The two-reaction mixture were placed in a Teflon-lined autoclave and heated at 120 °C for 12 h, then cooled to room temperature. The resultant rGO-Sn-HS-Pd$_1$ was purified with DI water and ethanol washes, followed by centrifugation, and dried at 75 °C for 24 h. Similar protocols were followed for rGO-Sn-HS-Pd$_2$ and rGO-Sn-HS-Pd$_3$, varying only the $PdCl_2$/PVP ratio in the reaction mixture. The Pd weight ratios in rGO$_2$-Sn-HS-Pd$_1$, rGO$_2$-Sn-HS-Pd$_2$, and rGO$_2$-Sn-HS-Pd$_3$ were theoretically set at 1.5 %, 3.0 %, and 4.5 %, respectively.

2.4. Crystal structure and morphological evaluation

The morphologies of the Sn-HS, rGO$_1$-Sn-HS, rGO$_2$-Sn-HS, rGO$_3$-Sn-HS, rGO$_2$-Sn-HS-Pd$_1$, rGO$_2$-Sn-HS-Pd$_2$, and rGO$_2$-Sn-HS-Pd$_3$ were examined using field emission scanning electron microscopy (FESEM) (JEOL JSM-7500F) and transmission electron microscopy (TEM) (JEM-2100F HR-TEM). The crystal structure was determined through powder X-ray diffraction (XRD) analysis using an X-Pert-pro instrument utilizing a CuKα1 (λ = 0.15406 nm) radiation source. Confocal Micro Raman spectra were acquired employing a Horiba Jobin-Yvon LabRam HR spectrometer equipped with a 17 mW internal He–Ne laser (632.8 nm

excitation). X-ray photoelectron spectroscopy studies were performed using an XPS, ESCALAB-MKII instrument with AlKα X-ray (hν = 1486.6 eV) as the excitation source.

2.5. Gas sensing characteristics

Gas sensing experiments were carried out using a target gas mixture of acetone and air, under constant gas flow rate of 300 sccm. To assess the influence of RH on gas sensing performance, experiments utilized humidified air as the target gas. This humidified air was prepared by precisely regulating the flow rates of two distinct gas streams: one of dry air and the other saturated with moisture via a bubbler system. The RH level of the resultant humidified air was accurately measured using a commercially available humidity sensor (DHT-11). The gas sensing experimental apparatus was integrated with a data acquisition system (GMC-1200, ATOVAC, Korea), alongside a temperature control unit, the MST-1000H from MSTECH, Korea. Data acquisition and monitoring were facilitated by the Keysight BenchVue software platform, interfaced with a Keysight 34461A digital multimeter, ensuring precise measurement and analysis of the sensor's electrical responses.

3. Results and discussion

3.1. Formation mechanism of porous SnO_2 nanospheres

Scheme 1 illustrates the formation mechanism of porous SnO_2 nanospheres using one step spray pyrolysis process without additional heat-treatment. Initially, droplets containing uniformly dispersed Sn salt, PVP, and PS beads were generated using an ultrasonic nebulizer (Scheme 1-①). These droplets were introduced into a vertical quartz tube reactor maintained at 700 °C, with air acting as the carrier gas. During this stage, the solvent evaporated, and the Sn salt decomposed, forming SnO_x/PVP/PS composite as an intermediate product (Scheme 1-②). Subsequently, the thermal decomposition of PS nanobeads occurred, leading to the creation of uniform pores within the powder structure. Moreover, PVP decomposed into carbon, forming a carbon matrix. This carbon matrix encasing the SnO_x nanoparticles hindered their aggregation, resulting in the formation of porous SnO_x/C nanospheres as a secondary intermediate (Scheme 1-③). Through continuous heating during the spray pyrolysis process, the carbon matrix combusted, producing CO_2, while SnO_x transformed into SnO_2, leading to the formation of nanospheres composed of pure SnO_2 nanoparticles (Scheme 1-④).

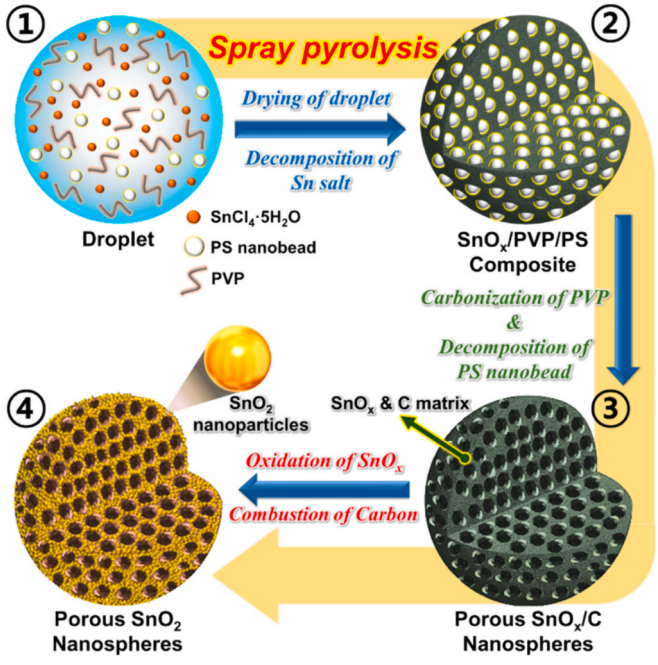

Scheme 1. Schematic illustrates the formation mechanism of porous SnO_2 nanospheres using one-step spray pyrolysis process.

3.2. Morphological analysis

Low-magnification FESEM images presents a detailed view of the synthesized Sn-HS, showing a uniform distribution of spherical structures without any other morphological features (Fig. 1**a-d**). High-magnification FESEM images revealed that the SnO_2 nanospheres had diameters ranging from 200 to 500 nm, with a distinctly rough surface morphology. Additionally, it was noted that the shells of the SnO_2 spheres were made up of clusters of several SnO_2 nanoparticles, each about 20 nm in diameter. The hollow nature of the spheres was clearly visible in images of broken SnO_2 spheres (Fig. 1**c, d**). The TEM images displayed the classic contrast profile, featuring a lighter center and darker edges, which is indicative of hollow structures (Fig. 1**e, f**). Additionally, the TEM images revealed the hierarchical mesoporous nature of the materials prepared. The diffraction rings in SAED were identified as corresponding to the (110), (101), (200), and (211) planes, consistent with the rutile SnO_2 crystal structure (Fig. 1**h**) [44]. The HRTEM images showed an interplanar spacing of 0.264 nm between adjacent lattice planes, matching the (1 0 1) planes of the rutile SnO_2 structure (Fig. 1**i**) [44]. Elemental mapping demonstrated the uniform distribution of tin (Sn) and oxygen (O) within the hollow structures (Fig. 1**j-k**). The EDS spectra quantitatively confirmed the elemental composition, with pronounced peaks attributable to Sn and O, in line with the expected stoichiometry of SnO_2.

Fig. 2**a, b** display FESEM images of the as-prepared rGO_2-Sn-HS-Pd_2. A clear hollow structure is visible in a fractured SnO_2 sphere, as shown in Fig. 2**b**. Similarly, the TEM images in Fig. 2**c, d** verify the hollow nature of the synthesized SnO_2 spheres, consistent with SEM findings. Fig. 2**e** features an HRTEM image of the rGO_2-Sn-HS-Pd_2, where the spacing between adjacent lattice planes is 0.26 nm [45]. This spacing indicates the (1 0 1) crystallographic planes of the rutile SnO_2 structure. In addition, spacings of 0.26 nm also match the (1 1 1) planes of the cubic Pd crystal structure [46]. This high-resolution image further clarifies that the multilayered rGO nanosheets act as a support for the SnO_2 and Pd NPs. Additional images at higher magnification show ultrafine Pd nanoparticles of various sizes within the rGO_2-Sn-HS-Pd_2 hybrid nanocomposite. The formation of Pd NPs in the rGO_2-Sn-HS-Pd_2 presents a noteworthy size differentiation, influenced by their proximity to SnO_2 and their interaction with the rGO nanosheets. Specifically, Pd NPs that form directly on the SnO_2 nanospheres are slightly larger, with a size of approximately 8 nm. This size increase can be attributed to the surface characteristics and energy states of the SnO_2 nanospheres, which may facilitate the aggregation of Pd atoms into larger nanoparticles. In contrast, Pd nanoparticles found near but not directly on the SnO_2 nanospheres exhibit smaller dimensions, with an average size of 5 nm. This size variation suggests a nuanced interplay between spatial proximity to SnO_2 and the dynamics of nanoparticle formation.

Furthermore, Pd NPs that are anchored on the rGO nanosheets display a markedly smaller size, ranging from 3 to 5 nm (Fig. 2**f-g**). The rings in the diffraction pattern can be indexed to the (110), (101), (200), and (211) planes of the rutile SnO_2 crystal structure (Fig. 2**h**) [44]. Elemental mapping showcases the uniform dispersion of Sn, O, Pd, and C elements throughout the rGO_2-Sn-HS-Pd_2 structure (Fig. 2**i-l**). The EDS spectra further quantitatively confirm the elemental composition of the nanocomposite (Fig. 2**m**). Pronounced peaks, characteristic of Sn, O, Pd, and C, corroborate the expected stoichiometry of rGO_2-Sn-HS-Pd_2. The EDS analysis of rGO_2-Sn-HS-Pd_1, rGO_2-Sn-HS-Pd_2, and rGO_2-Sn-HS-Pd_3 showed Pd weight ratios of 0.95 %, 1.72 %, and 4.25 %, respectively (**Fig. S2-S4**). EDS is a semi-quantitative technique that primarily detects elements within the interaction volume of the electron beam, which

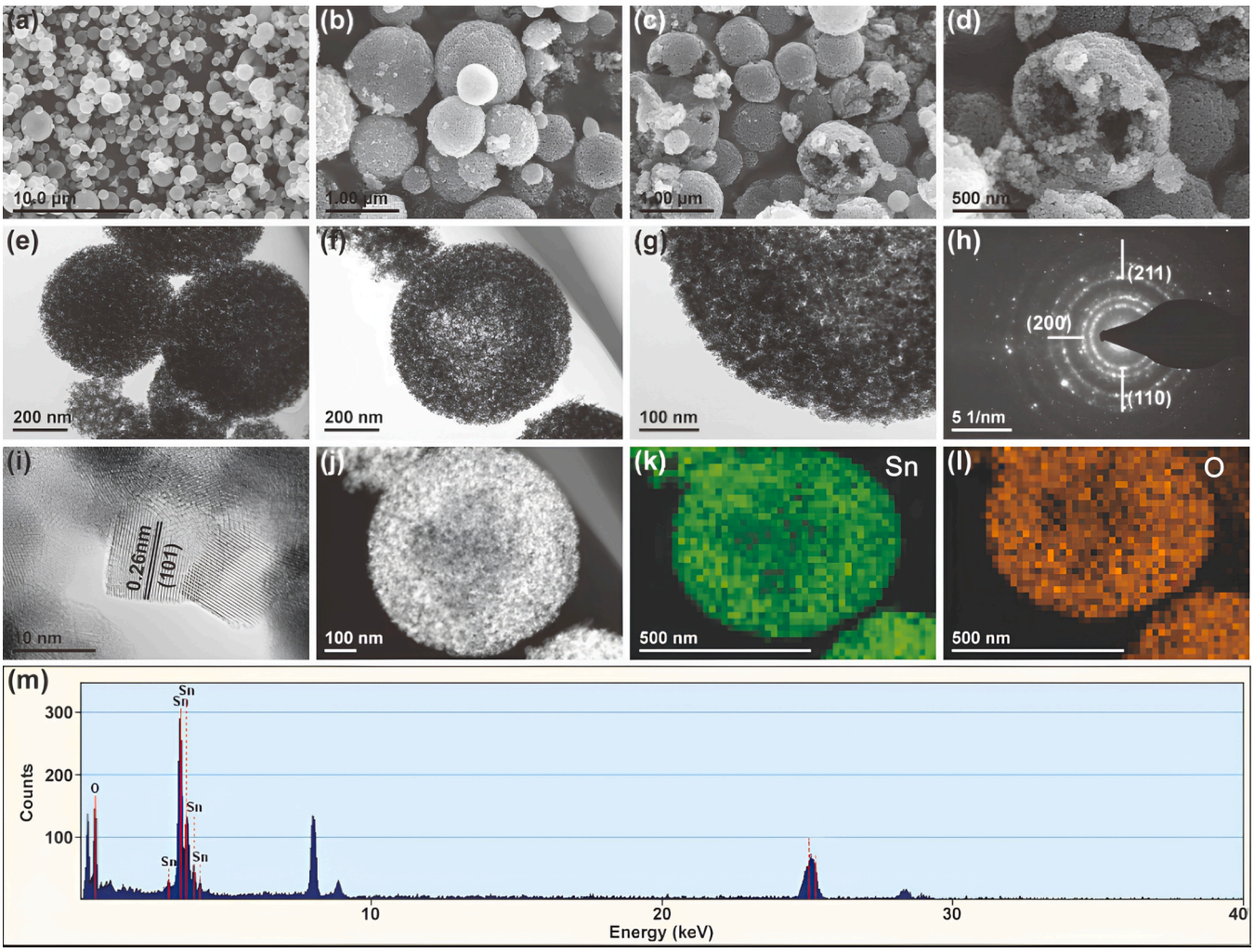

Fig. 1. Morphological analysis of the as-prepared Sn-HS in scanning and transmission mode. (a-d) FESEM images of the as-prepared Sn-HS at four different magnifications. (e-g) TEM images of the as-prepared Sn-HS at different magnifications. (h, i) SAED pattern and HRTEM image of the as-prepared Sn-HS. (j-m) Elemental mapping and energy dispersive spectrum of the as-prepared Sn-HS.

extends a few micrometers into the sample. However, EDS has limitations in detecting low-concentration elements with high accuracy and is also affected by matrix effects, leading to variations in the measured composition. Therefore, the actual weight ratios of Pd in the rGO-Sn-HS-Pd hybrid composite, as confirmed by Inductively Coupled Plasma (ICP) analysis, were found to be 1.62 %, 3.04 %, and 4.33 % in rGO_2-Sn-HS-Pd_1, rGO_2-Sn-HS-Pd_2, and rGO_2-Sn-HS-Pd_3, respectively. The Pd weight percentage was determined using ICP-MS (NexIon 1000, PerkinElmer), which provides highly accurate quantification of bulk elemental composition. Given the high accuracy and reliability of ICP for bulk elemental quantification, these values were considered the actual Pd content in the composites.

3.3. Crystal structure and phase purity analyses

The structural analysis of the synthesized compounds Sn-HS, rGO_1-Sn-HS, rGO_2-Sn-HS, rGO_3-Sn-HS, rGO_2-Sn-HS-Pd_1, rGO_2-Sn-HS-Pd_2, and rGO_2-Sn-HS-Pd_3 was carried out using X-ray diffraction (XRD) techniques. The XRD patterns for all samples confirmed the formation of the rutile phase of SnO_2, with no signs of other tin oxide phases such as SnO or orthorhombic SnO_2 (Fig. 3**a**). The diffraction peaks can be indexed to the identified for rutile SnO_2 were located at 2θ angles of 26.6, 33.9, 37.9, 51.8, 54.8, 57.8, 61.9, 64.9, 64.7, 65.9, 71.2, and 78.6°. These angles correspond to the (110), (101), (200), (211), (220), (002), (310), (112), (301), (202), and (321) planes of rutile SnO_2 (JCPDS no. 41–1445), respectively [47,48]. The smaller peaks observed around 31° and 45° can be attributed to the residual amount of metallic Sn, which remained from the synthesis process used to prepare SnO_2 hollow spheres. This minor residual Sn phase does not significantly affect the structural integrity or gas sensing performance of the composite. For the samples rGO_2-Sn-HS-Pd_1, rGO_2-Sn-HS-Pd_2, and rGO_2-Sn-HS-Pd_3, no distinct diffraction patterns related to palladium and rGO were detected, likely because the palladium and rGO content were below the XRD equipment's detection limit.

The Raman spectra for bare Sn-HS, rGO_1-Sn-HS, rGO_2-Sn-HS, rGO_3-Sn-HS, rGO_2-Sn-HS-Pd_1, rGO_2-Sn-HS-Pd_2, and rGO_2-Sn-HS-Pd_3 are illustrated in Fig. 3**b**. Specifically, the Raman spectrum of bare Sn-HS displays unique SnO_2 nanocrystal bands across the 200–1000 cm^{-1} spectrum. The detected Raman bands at 311, 636, and 774 cm^{-1} correspond to the E_g, A_{1g}, and B_{2g} vibrational modes of the rutile phase in SnO_2 crystals, respectively [49,50]. Additionally, the Raman spectra for rGO-Sn-HS and its Pd-doped variants (rGO_2-Sn-HS-Pd_1, rGO_2-Sn-HS-Pd_2, and rGO_2-Sn-HS-Pd_3) feature two prominent carbon-related bands between 1200–1800 cm^{-1}, representing the D and G bands of graphitic structure [51–53]. The D band, linked to the phonon k point of A_{1g} symmetry, indicates defect formation due to functional groups in the graphitic structure. Meanwhile, the G peak, associated with the E_{2g} phonon of sp_2-bonded carbon atoms, emphasizes the structural integrity

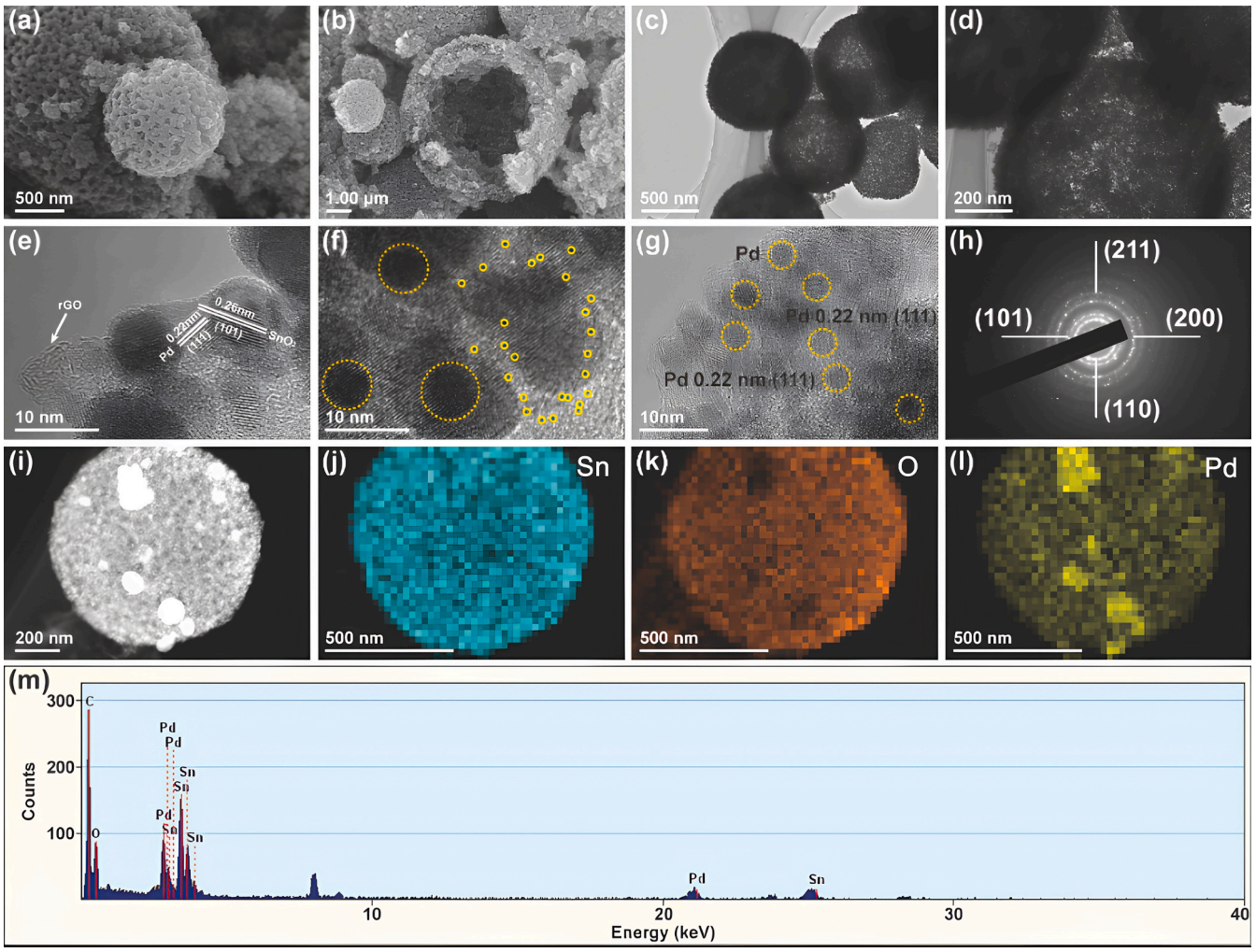

Fig. 2. Morphological Characterization of rGO_2-Sn-HS-Pd_2 via Electron Microscopy. (a, b) FESEM images of rGO_2-Sn-HS-Pd_2 at varying magnifications. (c, d) TEM images of rGO_2-Sn-HS-Pd_2 at two distinct magnifications. (e) HRTEM image of rGO_2-Sn-HS-Pd_2. (f-g) HRTEM images revealing SnO_2 nanoparticles alongside Pd nanoparticles of varying sizes, (h) SAED pattern of rGO_2-Sn-HS-Pd_2. (i-m) Elemental mapping and the energy dispersive spectrum of rGO_2-Sn-HS-Pd_2.

of graphitic domains within the samples.

Thermogravimetric analysis (TGA) was used to assess the thermal stability of the synthesized materials, namely Sn-HS, rGO_1-Sn-HS, rGO_2-Sn-HS and rGO_3-Sn-HS. The TGA curve for rGO-Sn-HS shows three distinct stages of mass loss (Fig. 3**c**). Initially, there is a decrease in mass up to 110 °C, which is due to the loss of water molecules adhering to the surface. This is followed by a mass loss between 110 °C and 300 °C, attributed to the removal of residual chemicals used in the synthesis of rGO-Sn-HS. The final stage of mass reduction is associated with the burning off rGO from the sample. In comparison, the TGA curve for Sn-HS displays only one significant mass loss event at 110 °C, suggesting the release of water molecules attached to the material. Beyond this point, the material shows excellent thermal stability, with no notable changes in mass with increasing temperature. The rGO content in the rGO_1-Sn-HS, rGO_2-Sn-HS and rGO_3-Sn-HS sample is estimated to be approximately 2, 4 and 6 wt%, as determined from the TGA data analysis.

The synthesized materials, including Sn-HS, rGO_1-Sn-HS, rGO_2-Sn-HS, rGO_3-Sn-HS, rGO_2-Sn-HS-Pd_1, rGO_2-Sn-HS-Pd_2, and rGO_2-Sn-HS-Pd_3, were analyzed for their surface area, pore size, and distribution using nitrogen adsorption/desorption measurements based on the Barret–Joyner–Halenda (BJH) method. The analysis revealed that the isotherms of these materials align with the classic Type IV classification and display a noticeable H_3-type hysteresis loop, indicating mesostructural properties (Fig. 3**d**). The observed hysteresis loops, ranging from low relative pressures ($0.3 < P/P0 < 0.8$) to higher ones ($0.8 < P/P0 < 1.0$), suggest a mixture of mesopores and micropores in the material's structure [53]. The Brunauer–Emmett–Teller (BET) specific surface areas were found to be 68 m^2/g for Sn-HS and 129 m^2/g for rGO_1-Sn-HS, 152 m^2/g for rGO_2-Sn-HS, 174 m^2/g for rGO_3-Sn-HS. For rGO_2-Sn-HS-Pd_1, rGO_2-Sn-HS-Pd_2, and rGO_2-Sn-HS-Pd_3, the surface areas increased to 159, 162, and 169 m^2/g, respectively. The observed increase in BET surface area following Pd incorporation can be attributed to several structural modifications within the rGO-Sn-HS framework. The incorporation of Pd nanoparticles may create additional interfacial voids between Sn-HS and rGO, further contributing to the increased surface area. Moreover, the formation of Pd nanoparticles on the surface may induce microstructural rearrangements, enhancing the total accessible surface area while maintaining the structural integrity of the composite. Furthermore, Pd incorporation may help stabilize the rGO structure by preventing restacking, thereby maintaining a more open and well-dispersed architecture. The interaction between Pd and Sn-HS may also promote further exfoliation of rGO sheets, leading to a more expanded structure with a higher specific surface area. The cumulative pore volumes for Sn-HS, rGO_1-Sn-HS, rGO_2-Sn-HS, rGO_3-Sn-HS, rGO_2-Sn-HS-Pd_1, rGO_2-Sn-HS-Pd_2, and rGO_2-Sn-HS-Pd_3 were measured at 0.452, 0.512, 0.919, 0.989, 1.051, 1.014, and 1.663 cm^3/g, respectively, demonstrating the significant porosity of these materials. Pore size analysis showed a predominant distribution within the 5–100 nm range, emphasizing the mesoporous nature of the materials (**Fig. S5**).

The synthesized materials were further analyzed using X-ray

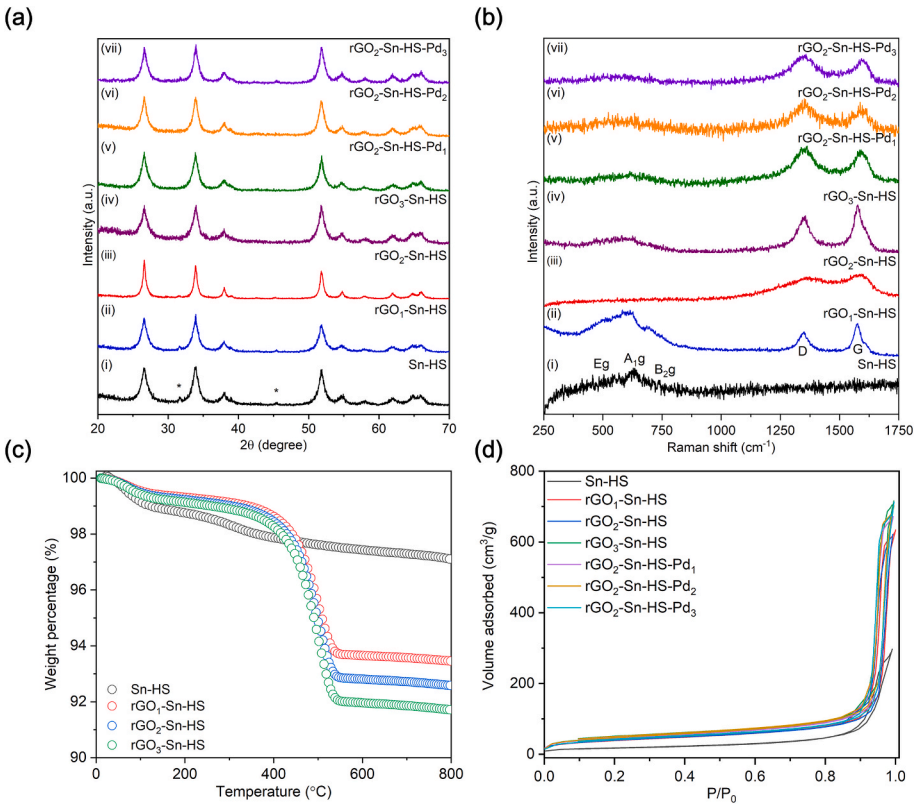

Fig. 3. Analytical characterization of the as-prepared nanocomposites. (a, b) Powder X-ray diffraction and micro-Raman spectra analyses of the as-prepared Sn-HS, rGO_1-Sn-HS, rGO_2-Sn-HS, rGO_3-Sn-HS, rGO_2-Sn-HS-Pd_1, rGO_2-Sn-HS-Pd_2, and rGO_2-Sn-HS-Pd_3 hybrid nanocomposite. (c) Thermogravimetry analysis of the as-prepared Sn-HS rGO_1-Sn-HS, rGO_2-Sn-HS and rGO_3-Sn-HS hybrid nanocomposite. (d) Nitrogen adsorption–desorption isotherm analysis of the as-prepared Sn-HS, rGO_1-Sn-HS, rGO_2-Sn-HS, rGO_3-Sn-HS, rGO_2-Sn-HS-Pd_1, rGO_2-Sn-HS-Pd_2, and rGO_2-Sn-HS-Pd_3 hybrid nanocomposite.

photoelectron spectroscopy (XPS) to determine their chemical composition and electronic states. The analysis showed clear photoelectron peaks for O 1 s, Sn 3d, Pd 3d, and C 1 s core levels (Fig. 4**a**). Fig. 4**b** shows detailed Pd 3d core level spectra for rGO_2-Sn-HS-Pd_1, rGO_2-Sn-HS-Pd_2, and rGO_2-Sn-HS-Pd_3, clearly separating the Pd $3d_{5/2}$ and Pd $3d_{3/2}$ peaks by 5.2 eV [54]. This separation reveals the existence of both Pd^0 and Pd^{2+} species, suggesting the formation of PdO [55]. The tin (Sn) 3d spectral line splits into Sn $3d_{5/2}$ and Sn $3d_{3/2}$ core levels for all samples, depicted in Fig. 4**c**. The Sn $3d_{5/2}$ peaks for the samples Sn-HS, was recorded at binding energy of 486.85, while the Sn $3d_{3/2}$ peaks were found at 494.7, respectively [56,57]. Further analysis showed that the presence of palladium nanoparticles causes a shift in the Sn $3d_{5/2}$ peak towards higher binding energies.

This indicates an increase in ionosorbed oxygen species on the SnO_2 surface, likely due to the transfer of oxygen species from the palladium to the oxide, resulting in an oxygen-enriched surface layer on the rGO-Sn-HS-Pd samples. The high-resolution O 1 s core-level spectra, were analyzed through deconvolution to differentiate among various oxygen species based on their oxidation states (Fig. 4**d**). Peaks observed at 530 eV were associated to lattice oxygen, while those at 532 and 533.5 eV were identified with chemisorbed (for example, O^-, O_2^-, O_2^{2-}) and physiosorbed oxygen species, respectively [12,51]. The notable prominence of peaks related to chemisorbed oxygen species in the Pd-doped samples highlights a significant increase in ionosorbed oxygen on the SnO_2 surface, a phenomenon attributed to the transfer of oxygen from noble metal centers through spill-over effect. This enrichment of the surface layer with oxygen is believed to potentially improve the gas-sensing capabilities of the samples rGO_2-Sn-HS-Pd_1, rGO_2-Sn-HS-Pd_2, and rGO_2-Sn-HS-Pd_3, as indicated by the higher intensity and area under the curves of these specific species.

3.4. Acetone sensing analyses

The methodologies employed for the fabrication and characterization of the gas sensors are comprehensively explained in the supplementary information. To ensure that the structures remained intact in the sensor device, we conducted FESEM analysis after coating the sample on the interdigitated electrodes. The FESEM images confirm that the morphology and structural characteristics of the material remain unchanged after the coating process, indicating that the grinding step did not adversely affect the integrity of the nanostructures (**Fig. S6**). The sensing response (S_R) of the sensor is quantitatively defined by Equ. (1).

$$SR = \frac{R_g}{R_a} \quad (1)$$

where R_a denotes the resistance of the sensor when exposed to ambient air, and R_g represents the sensor's resistance in the presence of the target gas. It is well established that the chemical kinetics of acetone sensing on the SnO_2 surface involve the release of electrons into the conduction band, followed by the conversion of acetone into CO_2 and H_2O. This process entails the adsorption of acetone molecules onto the SnO_2 surface, where they react and decompose, liberating electrons into the material's conduction band, thereby enhancing its conductivity. Subsequently, the decomposed acetone molecules are transformed into CO_2 and H_2O, which are desorbed from the surface, completing the sensing mechanism (Fig. 5**a**).

The observed decrease in sensor resistance with increasing temperature can be attributed to the negative temperature coefficient characteristic of metal oxide-based sensors. This phenomenon arises from the thermally activated release of charge carriers, which enhances their mobility and reduces resistivity. Such behavior is critical for sensor performance, as it impacts sensitivity of the sensor (Fig. 5**b**). The

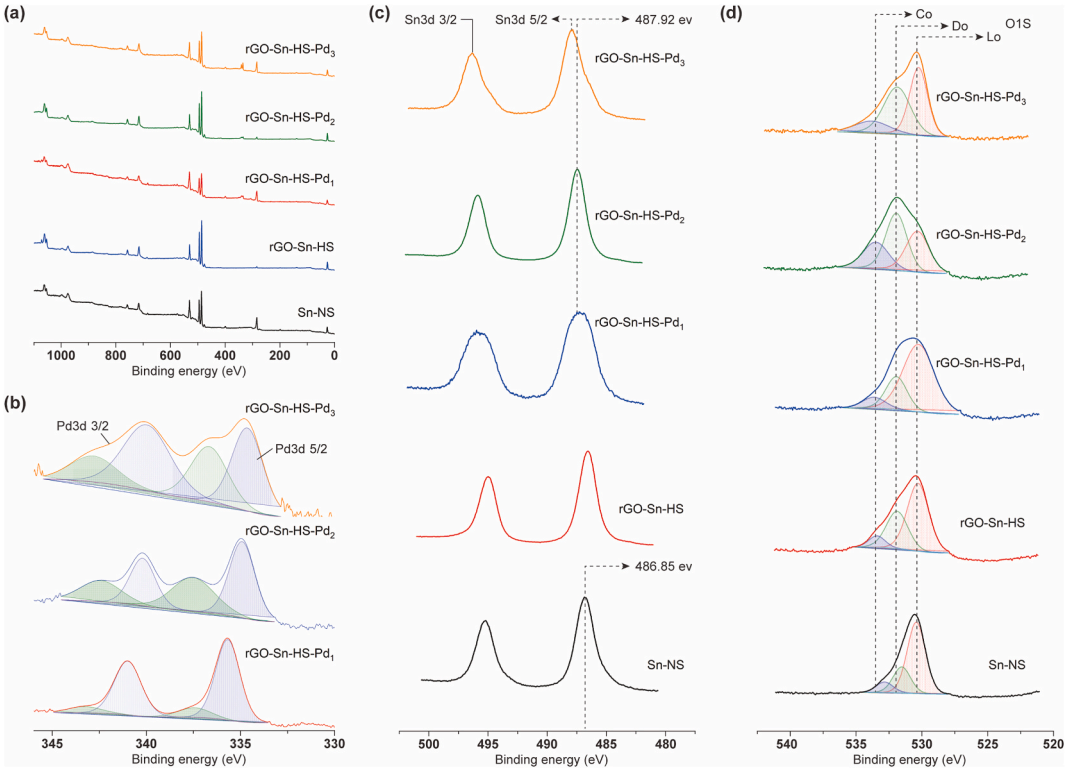

Fig. 4. X-ray photoelectron spectra analysis of the as-prepared nanocomposites. (a) Survey spectra of the as-prepared Sn-HS, rGO_2-Sn-HS, rGO_2-Sn-HS-Pd_1, rGO_2-Sn-HS-Pd_2, and rGO_2-Sn-HS-Pd_3 hybrid nanocomposite. (b) High-resolution Pd3d core-level spectra, displaying spin–orbit splitting, for the rGO_2-Sn-HS-Pd_1, rGO_2-Sn-HS-Pd_2, and rGO_2-Sn-HS-Pd_3 hybrid nanocomposite. (c, d) High-resolution Sn3d and O1s core-level spectra, illustrating spin–orbit splitting, for the Sn-HS, rGO_2-Sn-HS, rGO_2-Sn-HS-Pd_1, rGO_2-Sn-HS-Pd_2, and rGO_2-Sn-HS-Pd_3 hybrid nanocomposite.

acetone sensing performance of sensors based on Sn-HS, rGO_1-Sn-HS, rGO_2-Sn-HS, rGO_3-Sn-HS, rGO_2-Sn-HS-Pd_1, rGO_2-Sn-HS-Pd_2, and rGO_2-Sn-HS-Pd_3 was evaluated by measuring their responses to 5 ppm of acetone across a range of operating temperatures (175 °C to 275 °C), as shown in Fig. 5**c and** Fig. S7**a**. It was observed that the sensor response to acetone increased with the operating temperature, displaying a volcano-shaped curve, with an optimal temperature identified at 250 °C for all samples. Quantitatively, we measured the responses of sensors based on Sn-HS, rGO_1-Sn-HS, rGO_2-Sn-HS, rGO_3-Sn-HS, rGO_2-Sn-HS-Pd_1, rGO_2-Sn-HS-Pd_2, and rGO_2-Sn-HS-Pd_3 to 5 ppm acetone at various temperatures (175, 200, 225, 250, and 275 °C).

The measured responses were as follows: for Sn-HS, the responses were 2.824, 4.654, 6.439, 8.132, and 7.207; for rGO_1-Sn-HS 3.646, 6.187, 9.761, 11.108 and 10.684; for rGO_2-Sn-HS, they were 5.745, 8.334, 12.983, 15.434, and 12.445; for rGO_3-Sn-HS, the response were 4.806, 7.418, 11.742, 13.068 and 11.464; for rGO_2-Sn-HS-Pd_1, the responses were 9.711, 16.881, 28.708, 47.221, and 38.442; for rGO_2-Sn-HS-Pd_2, they were 15.677, 27.261, 41.228, 59.785, and 48.667; and for rGO_2-Sn-HS-Pd_3, the responses were 14.256, 22.552, 36.288, 52.118, and 42.881, respectively. Our analysis of these sensing responses revealed that the optimal level of rGO is 4 wt% and Pd incorporation is 3 wt%, which is supported by the highest response of 59.785 to 5 ppm acetone observed with the rGO_2-Sn-HS-Pd_2 sensor. This configuration showed superior performance, yielding responses that were approximately 7.35, 3.87, 1.27, and 1.15 times higher than those of the bare Sn-HS, rGO_1-Sn-HS, rGO_2-Sn-HS, rGO_3-Sn-HS, rGO_2-Sn-HS-Pd_1, rGO_2-Sn-HS-Pd_2, and rGO_2-Sn-HS-Pd_3 sensors, respectively.

The efficacy of the sensor is intricately related to the activation energy of the sensing materials, with materials exhibiting lower activation energies typically demonstrating superior electrochemical sensing capabilities. To quantitatively evaluate the activation energies of the fabricated sensors, the Arrhenius equation was employed, represented as follows:

$$S = S_0 \exp\left(\frac{E_a}{2k_B T}\right) \quad (2)$$

Here, S denotes the sensing response, S_0 is a pre-exponential factor, E_a represents the activation energy, T is the absolute temperature, and k_B is the Boltzmann constant. The relationship between the sensing response and temperature was graphically depicted in Arrhenius plots, which exhibited an exhibited linear correlation, as shown in Fig. 5**d and** Fig. S7**b**. By analyzing the slope of the logarithm of the sensing response ($\log(S_R)$) versus the inverse of temperature (1000/T), the activation energies were determined. The activation energy of the sensors based on Sn-HS, rGO_1-Sn-HS, rGO_2-Sn-HS, rGO_3-Sn-HS, rGO_2-Sn-HS-Pd_1, rGO_2-Sn-HS-Pd_2, and rGO_2-Sn-HS-Pd_3 was found to be approximately 0.411, 0.407, 0.399, 0.404, 0.378, 0.362, and 0.367 eV, respectively. The rGO_2-Sn-HS-Pd_2 sensor showcased the lowest activation energy, indicative of its enhanced electrochemical performance relative to the other sensor configurations.

The sensor resistance and response of all sensors at the optimal sensing temperature of 250 °C toward 5 ppm acetone are shown in Fig. 5**e**. Upon exposure to acetone, the sensor resistance decreased, indicating gas interaction, and recovered to its baseline once the gas was turned off. Similarly, the sensor response increased during acetone exposure and returned to its initial value after the gas was removed, demonstrating a reversible sensing behavior. Subsequently, the dynamic acetone-sensing performance of Sn-HS, rGO_1-Sn-HS, rGO_2-Sn-HS, rGO_3-Sn-HS, rGO_2-Sn-HS-Pd_1, rGO_2-Sn-HS-Pd_2, rGO_2-Sn-HS-Pd_3 was evaluated over an acetone concentration range of 1 to 5 ppm at an operating temperature of 250 °C. Consistent with expectations, an increase in acetone concentration correlated with an enhanced sensing response. The sensors fabricated from Sn-HS, rGO_1-Sn-HS, rGO_2-Sn-HS, rGO_3-Sn-HS, rGO_2-Sn-HS-Pd_1, rGO_2-Sn-HS-Pd_2, and rGO_2-Sn-HS-Pd_3 exhibited

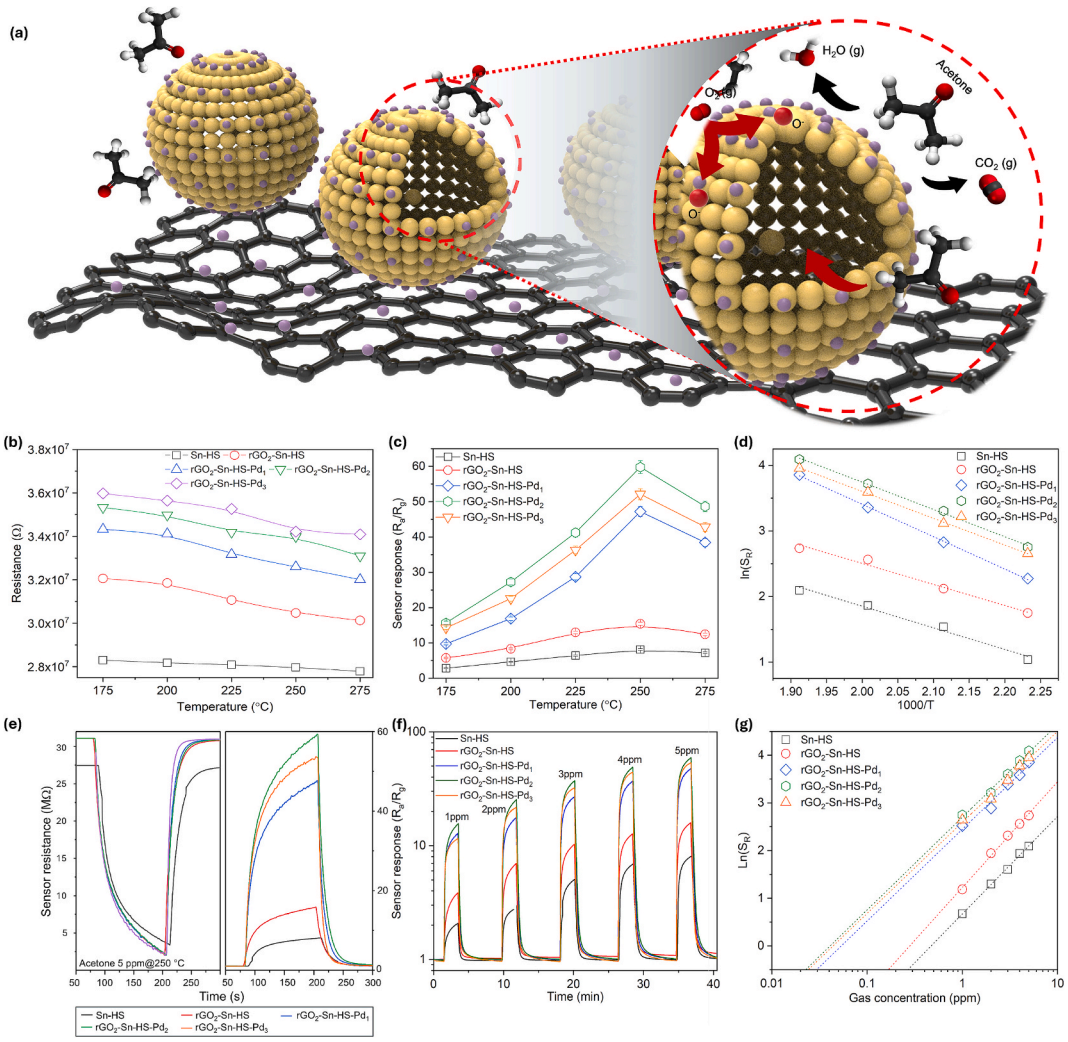

Fig. 5. Acetone sensing characteristics of the fabricated sensors based on Sn-HS, rGO_2-Sn-HS, and rGO_2-Sn-HS-Pd_1, rGO_2-Sn-HS-Pd_2, and rGO_2-Sn-HS-Pd_3. (a) Schematic images of acetone sensing mechanism of rGO_2-Sn-HS-Pd hybrid nanocomposites. (b) Sensor resistance at different temperature. (c) Sensor response as a function of operating temperature for Sn-HS, rGO_2-Sn-HS, and rGO_2-Sn-HS-Pd_1, rGO_2-Sn-HS-Pd_2, and rGO_2-Sn-HS-Pd_3 toward 5 ppm acetone. (d) Arrhenius plots showcasing the activation energy for acetone sensing across different sensor compositions. (e) Sensor resistance and response at the optimal sensing temperature of 250 °C toward 5 ppm acetone. (f) Dynamic response curves over time for various acetone concentrations (1, 2, 3, 4, and 5 ppm) at 250 °C. (g) Calibration curves indicating the sensitivity of the sensors at different acetone concentrations.

responses of 1.92, 3.652, 4.976, 6.943, 8.132; 2.448, 5.262, 6.848, 9.431, 11.108; 3.906, 6.973, 10.126, 12.934, 15.434; 3.688, 6.851, 9.561, 10.987, 13.562; 12.437, 17.995, 29.663, 36.034, 47.221; 15.564, 24.865, 36.718, 48.728, 59.785; 11.534, 21.795, 32.271, 43.743, and 52.118, respectively, across acetone concentrations of 1, 2, 3, 4, and 5 (as shown in Fig. 5**f**, Fig. S8**a**, Fig. S9**a**). All fabricated sensors demonstrated excellent linear correlations between the logarithm of the sensor response and gas concentrations, aligning with the empirical models proposed for semiconductor gas sensors (Fig. 5**g**, Fig. S8**b**, Fig. S9**b**). Notably, the rGO_2-Sn-HS-Pd_2-sensor showcased a remarkably low detection threshold, reaching as low as 220 ppb. This sensitivity far exceeds the requirements for industrial monitoring applications and holds significant promise for medical diagnostics, including diabetes detection, where the capability to identify acetone concentrations well below the critical threshold of 1.8 ppm is crucial. The rGO_2-Sn-Pd_2 sensor exhibits an excellent sensing response compared to other sensor configurations. Therefore, further analyses, including stability, repeatability, selectivity, effect of humidity, and breath sensing evaluation, were conducted using the rGO_2-Sn-Pd_2 sensor to comprehensively assess its performance for practical applications.

The enhancement in acetone detection by the rGO_2-Sn-HS-Pd_2 sensor is attributed to three primary mechanisms. First, the sensor's hollow structural design substantially enhances the number of reactive sites by facilitating the diffusion of gas molecules into the sensor's hollow spheres. Moreover, the strategic distribution of Sn-HS and ultrafine Pd-NPs across the rGO sheets, forming multiheterojunctions within the rGO_2-Sn-HS-Pd composites, significantly influences sensor functionality (Scheme 2**a**). Before the chemisorption of atmospheric oxygen species, the rGO − SnO_2 heterojunction is initially ohmic, attributed to the disparate work functions of the materials involved ($\Phi G > \Phi SnO_2$), leading to electron accumulation on the Sn-HS surface to equilibrate the Fermi levels. Subsequent electron migration towards chemisorbed O_2 species creates a depletion region at the heterojunction characterized by a specific width (W_{dO}) and barrier height (Φ_{bO}), consequently increasing the sensor's resistance. As discussed earlier, XPS analysis reveals that the rGO_2-Sn-HS-Pd_2 configuration exhibits enhanced chemisorption of oxygen molecules on its surface, leading to an increase in baseline resistance compared to other configurations, as demonstrated **in** Fig. 6**a**. This elevated oxygen adsorption plays a crucial role in improving the gas-sensing performance of the sensor. A key factor contributing to the enhanced sensing ability of the rGO_2-Sn-HS-Pd_2 sensor is the spillover effect induced by Pd nanoparticles. Pd nanoparticles act as catalytic

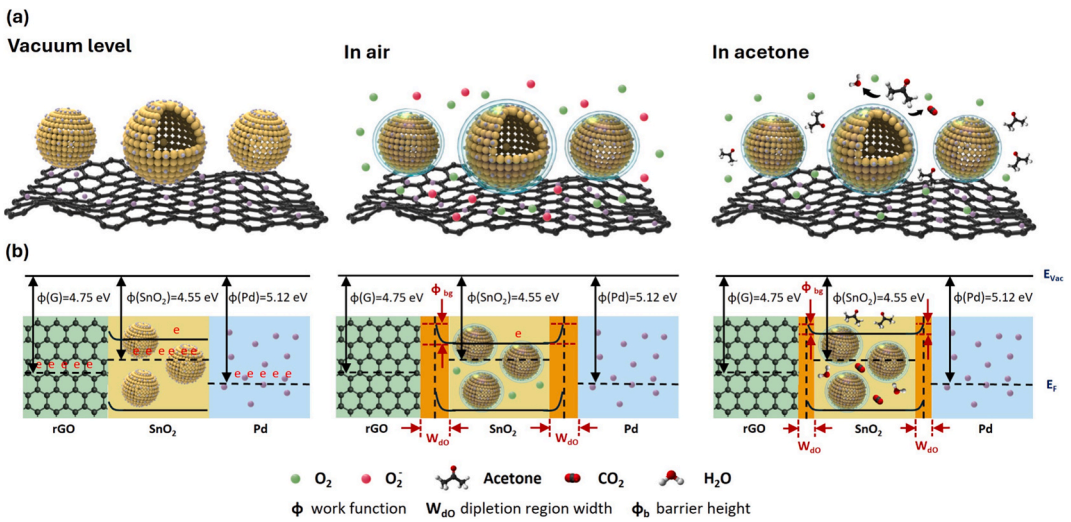

Scheme 2. (a) Schematic representation of the physical models, illustrating the structural configuration and distribution of components within the rGO_2-Sn-HS-Pd_2 sensor system, and (b) an energy band diagram that elucidates the acetone sensing mechanism.

sites, where incoming oxygen molecules are initially adsorbed and subsequently dissociated into highly reactive oxygen species (O_2^-, O^-). These reactive species then migrate to the surrounding Sn-HS-rGO matrix, increasing the ionosorption of oxygen and facilitating more effective charge transfer. This spillover effect not only increases the active surface sites for acetone adsorption but also accelerates the redox reaction involved in the sensing mechanism. Additionally, the synergistic catalytic effect of rGO and the optimized concentration of Pd nanoparticles further enhances the adsorption–desorption kinetics of acetone molecules. The presence of Pd promotes efficient electron exchange between the sensing material and the analyte gas, leading to a more pronounced sensing response. Moreover, the incorporation of Pd reduces the activation energy required for acetone oxidation, thereby improving surface reactivity and enhancing the electrochemical oxidation process. This results in a higher response, faster recovery, and improved selectivity toward acetone vapor. Furthermore, the increase in Pd content up to rGO_2-Sn-HS-Pd_2 leads to a progressive enhancement in sensing performance due to the increased availability of catalytic active sites, stronger spillover effects, and improved charge transfer interactions. However, a further increase in Pd content beyond the optimal level, as in rGO_2-Sn-HS-Pd_3, results in a decline in sensing performance. This reduction can be attributed to the weakening spillover effect, which reduces the number of catalytically active sites, limits oxygen adsorption, and hinders efficient charge transfer within the sensing matrix. Additionally, excessive Pd loading can lead to partial coverage of reactive Sn-HS sites, thereby suppressing the active role of Sn-HS in gas sensing. As a result, the optimal Pd content in rGO_2-Sn-HS-Pd_2 achieves a balance between catalytic activity, charge transfer efficiency, and gas diffusion, leading to superior sensing performance compared to rGO_2-Sn-HS-Pd_3. The presence of heterojunctions between SnO_2 and rGO serves as conduits for electron migration, expediting the sensor's response during acetone detection. Within an acetone environment, dissociated acetone species preferentially bind to active sites present at the graphene-metal oxide and Pd interfaces, including vacancies, line defects, and areas of strong electronic interaction between graphene and metal oxides. The adsorbed acetone reacts with molecular oxygen species, triggering electron transfer to the Sn-HS conduction band. Consequently, rGO receives electrons from adjacent Sn-HS, functioning as electron transporters, leading to a significant reduction in both depletion width and potential barrier height, as illustrated in the energy band model (Scheme 2**b**). Collectively, these attributes of the rGO_2-Sn-HS-Pd_2 composite synergize to enhance acetone detection capabilities. Besides, all sensor configurations exhibited rapid response times (less than 50 s) and recovery times (less than 70 s), demonstrating the efficiency of the hierarchical mesoporous structure in facilitating the diffusion of gas molecules into the sensing layers, thereby precipitating a swift decrease in resistance, and recovering back to their original resistance.

The rGO_2-Sn-HS-Pd_2-based sensor exhibited exceptional repeatability in detecting acetone concentrations within the 3 to 15 ppm range, with its sensing response in direct proportion to the gas concentration at an operational temperature of 250 °C. When the acetone concentration was reduced from 15 to 3 ppm, the sensor promptly reverted to its sensor response value, affirming its dependable performance across both detection and recovery stages (Fig. 6**b**).

To further assess its reliability, the stability of the rGO_2-Sn-HS-Pd_2 sensor was evaluated over six cycles of exposure to 5 ppm of acetone. The results demonstrated consistent repeatability in sensor response with minimal deviation, specifically a sensing response (SR) of 59.72 ± 2.12 (Fig. 6**c**). The sensing response of the rGO_2-Sn-HS-Pd_2 sensor toward 5 ppm acetone was found to be increased with decreasing the humidity (Fig. 6**d**). The detailed experimental protocol for RH control during sensing measurements is provided in the supporting information. To evaluate the long-term stability, the sensor's response to 5 ppm acetone was monitored at 250 °C over an extended period under identical operating conditions at periodic time intervals. As shown in **Fig. S10**, the sensor exhibited remarkable stability, maintaining a consistent response with minimal deviation for up to 60 days, demonstrating its long-term reliability for prolonged use.

The selectivity rGO_2-Sn-HS-Pd_2 sensor against a variety of gas molecules, including acetone, ethanol, ammonia, carbon monoxide, nitrogen dioxide, sulfur dioxide, hydrogen and hydrogen sulfide was investigated at 250 °C. These gases were selected based on their relevance to exhaled breath analysis and environmental monitoring. Acetone is the primary analyte, while ethanol and ammonia are common breath components that may interfere with acetone detection. Hydrogen is a biomarker for digestive disorders such as lactose intolerance and small intestinal bacterial overgrowth, and nitric oxide is associated with asthma diagnosis. Carbon monoxide and sulfur dioxide are key air pollutants, while hydrogen sulfide, though present in trace amounts in breath, is linked to halitosis and gastrointestinal disorders. Remarkably, the sensor displayed a pronounced preference for acetone, registering a sensing response (S_R) of approximately 59 at a concentration of 5 ppm. This response is notably superior to its reactivity with other gases, as evidenced by the following S_R values: ethanol (S_R = 2.08 at 10 ppm), ammonia (S_R = 3.46 at 10 ppm), carbon monoxide (S_R = 2.75 at 10 ppm), nitrogen dioxide (S_R = 4 at 10 ppm), sulfur dioxide (S_R = 5.8 at

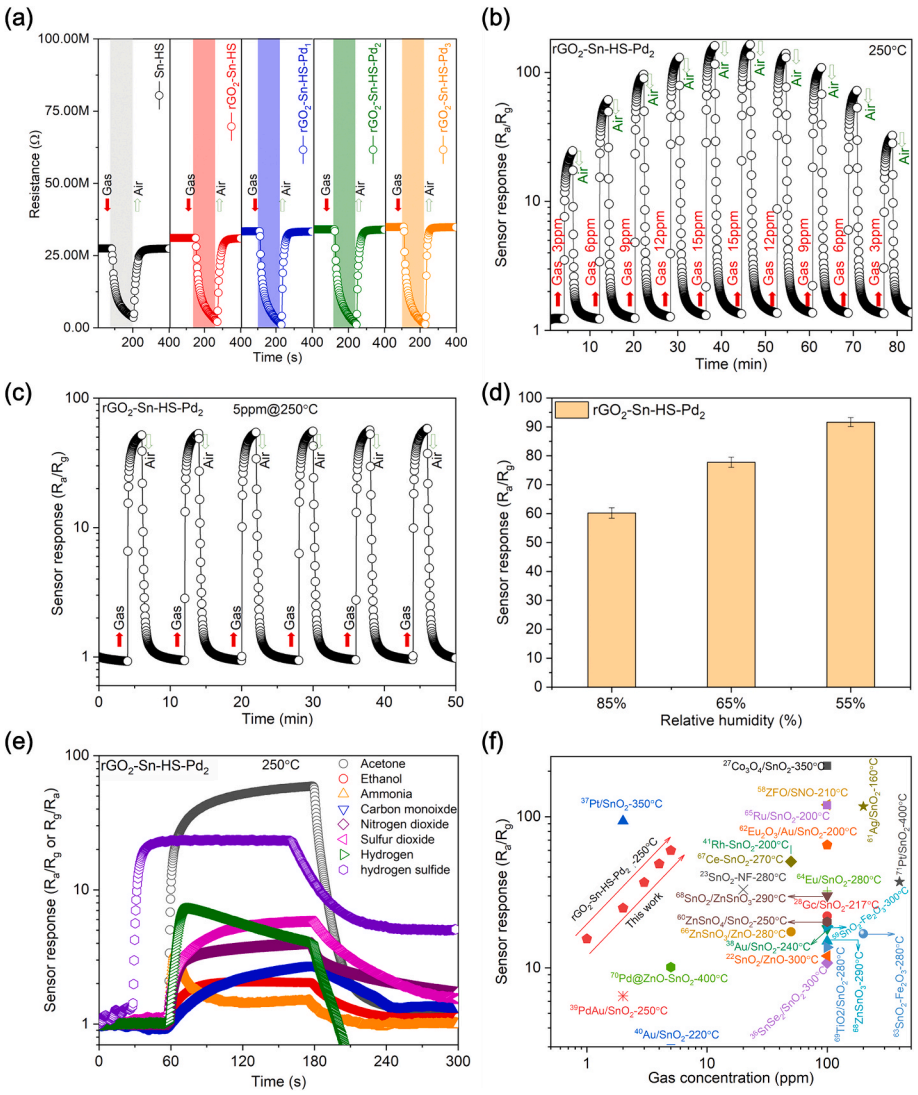

Fig. 6. (a) Resistance of sensors based on Sn-HS, rGO_2-Sn-HS, rGO_2-Sn-HS-Pd_1, rGO_2-Sn-HS-Pd_2, and rGO_2-Sn-HS-Pd_3 towards 5 ppm acetone at 250 °C. (b) Repeatability of the rGO_2-Sn-HS-Pd_2 sensor towards 1–5 ppm and 5–1 ppm acetone at 250 °C. (c) Stability of the rGO_2-Sn-HS-Pd_2 sensor towards 5 ppm acetone at 250 °C. (d) Effect of humidity on the sensing performance of the rGO_2-Sn-HS-Pd_2 sensor towards 5 ppm acetone at different relative humidity at 250 °C. (e) Selectivity of the rGO_2-Sn-HS-Pd_2 sensor towards 5 ppm acetone and 10 ppm other interfering gases. (f) Comparison of the sensing response of the rGO_2-Sn-HS-Pd_2 sensor with that of other reported SnO_2-based hybrid nanocomposite sensors.

10 ppm), hydrogen (S_R = 7.27 at 10 ppm) and hydrogen sulfide (S_R = 23.58 at 10 ppm) (Fig. 6**e**). The proposed rGO_2-Sn-HS-Pd_2 sensor demonstrates an exceptional sensing response at relatively low concentrations of acetone and at low operating temperatures, surpassing the performance of previously reported sensors based on SnO_2 hybrid nanocomposites [22,23,27,28,36–41,58–70] (Fig. 6**f**).

The rGO_2-Sn-HS-Pd_2 sensor was employed to detect acetone in exhaled human breath, serving as a potential biomarker for diabetes. Breath samples were collected from seven healthy individuals using Tedlar bags. To each sample, 2 ppm of acetone were added to simulate a diabetic breath profile. Fig. 7**a** illustrates an electronic nose system that incorporates the rGO_2-Sn-HS-Pd_2 sensor, designed for the real-time diagnosis of diabetes. The accompanying flowchart details the experimental procedure, which includes acetone calibration, breath sample collection, sensor signal generation, and subsequent data analysis, as shown in Fig. 7**b**. The scatter plot depicted in Fig. 7**c,d** clearly demonstrates the sensor's capacity to discriminate between normal breath and breath simulated with acetone for diabetic conditions. This significant distinction in sensor responses indicates the rGO_2-Sn-HS-Pd_2 sensor's high selectivity and sensitivity to acetone, relative to other interfering gases present in exhaled breath. Furthermore, the PCA clearly visualizes the sensor array's ability to differentiate between the two sample states, with a pronounced separation between the clusters for healthy and simulated diabetic breath. The results demonstrate the rGO_2-Sn-HS-Pd_2 sensor's adeptness at detecting diabetic biomarkers. This proficiency underscores the sensor's potential as a platform for the advancement of non-invasive diagnostic methodologies in biomedical fields.

4. Conclusion

In conclusion, a highly selective and sensitive acetone sensor was developed by dual sensitization of SnO_2 hollow spheres with rGO and Pd NPs. The SnO_2 hollow spheres were synthesized using the spray pyrolysis method. These were then dual sensitized with rGO and Pd NPs via a subsequent hydrothermal method. Comprehensive materials characterization employing various analytical techniques confirmed the successful formation of hollow spheres and the hybrid nanocomposite. The sensor array, comprising Sn-HS, rGO_1-Sn-HS, rGO_2-Sn-HS, rGO_1-Sn-HS, rGO_2-Sn-HS-Pd_1, rGO_2-Sn-HS-Pd_2, and rGO_2-Sn-HS-Pd_3, demonstrated excellent sensitivity to acetone at 250 °C. Notably, the rGO_2-Sn-HS-Pd_2

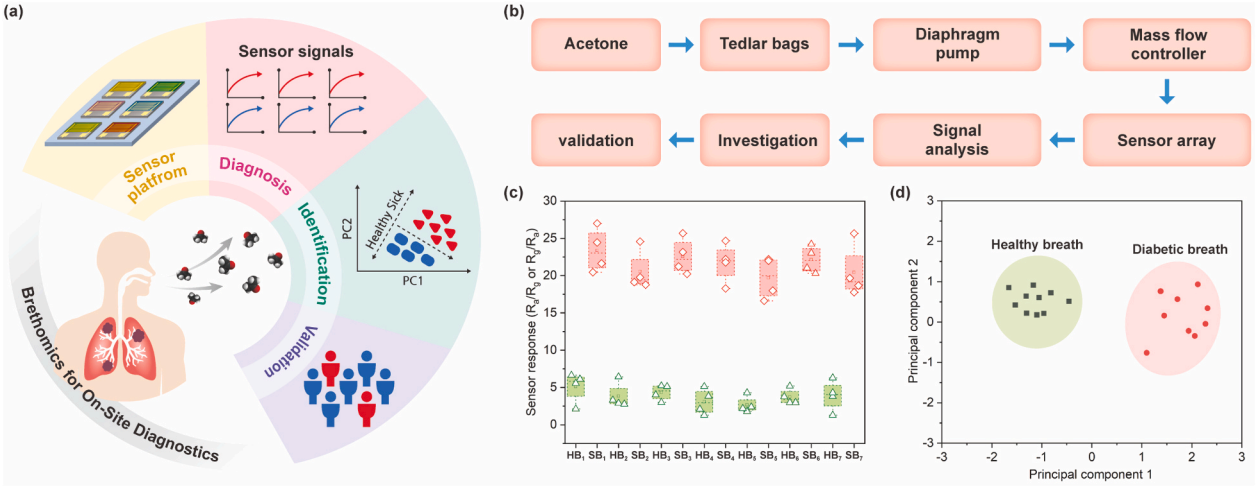

Fig. 7. Breath sensing analysis. (a) A schematic representation of the breathomic analysis using an electronic nose system that utilizes the rGO_2-Sn-HS-Pd_2 sensor. (b) A flowchart detailing the methodological steps undertaken during the experimental breath analysis. (c) A scatter plot demonstrating the rGO_2-Sn-HS-Pd_2 sensor's differential response to healthy breath and breath simulated with 2 ppm acetone. (d) A principal component analysis (PCA) of the data acquired from the rGO_2-Sn-HS-Pd_2 sensor array, which distinctly segregates healthy from diabetic breath.

sensor exhibited a superior sensing response, approximately 7.35, 3.87, 1.27, and 1.15 times greater than that of the bare Sn-HS, rGO_2-Sn-HS-Pd_1, rGO_2-Sn-HS-Pd_2, and rGO_2-Sn-HS-Pd_3 sensors, respectively. The rGO_2-Sn-HS-Pd_2 sensor also presented a lower activation energy of 0.362 eV, signifying its improved electrochemical performance in comparison to the other sensor variants. Additionally, the rGO_2-Sn-HS-Pd_2 sensor demonstrated exemplary stability, repeatability, and long-term durability, affirming the practical applicability of the sensor design. In terms of selectivity, the rGO_2-Sn-HS-Pd_2 sensor displayed outstanding discrimination towards acetone over other potential interfering gases, including ethanol, ammonia, carbon monoxide, nitrogen dioxide, sulfur dioxide, and hydrogen. Utilizing a sensor array of rGO_2-Sn-HS-Pd_2, acetone-enriched breath was clearly differentiated from healthy breath via PCA analysis. These findings validate the rGO_2-Sn-HS-Pd_2 sensor's capability as an innovative sensing platform for exhaled breath analyzers, with potential applications in the diagnosis of metabolic disorders.

CRediT authorship contribution statement

Arunkumar Shanmugasundaram: Writing – review & editing, Writing – original draft, Visualization, Validation, Project administration, Methodology, Investigation, Funding acquisition, Formal analysis, Data curation, Conceptualization. **Kun Woo Baek:** Methodology, Formal analysis, Data curation, Conceptualization. **Changung Paeng:** Methodology, Formal analysis, Data curation. **Longlong Li:** Formal analysis, Data curation. **Goeun Cha:** Formal analysis, Data curation. **Jonghyeon Woo:** Formal analysis, Data curation. **Dong-Su Kim:** Formal analysis, Data curation. **Changyong Yim:** Visualization, Validation, Resources, Methodology, Formal analysis, Data curation. **Jongsung Park:** Formal analysis, Data curation. **Jung Sang Cho:** Project administration, Resources, Methodology, Funding acquisition, Formal analysis, Data curation, Conceptualization. **Dong-Weon Lee:** Writing – review & editing, Visualization, Supervision, Project administration, Resources, Conceptualization, Funding acquisition, Investigation.

Declaration of competing interest

The authors declare that they have no known competing financial interests or personal relationships that could have appeared to influence the work reported in this paper.

Acknowledgements

This work was supported by the National Research Foundation of Korea (NRF) grant funded by the Korea government (RS-2023-00250781) and the National Research Foundation of Korea (NRF) grant funded by the Korea government (MSIT) (2020R1A5A8018367 and RS-2021-NR060108) and National Research Foundation of Korea (NRF) and the Commercialization Promotion Agency for R&D Outcomes (COMPA) funded by the Ministry of Science and ICT (RS-2023-00217581).

Appendix A. Supplementary material

Supplementary data to this article can be found online at https://doi.org/10.1016/j.apsusc.2025.162959.

Data availability

Data will be made available on request.

References

[1] P. Mochalski, G. Shuster, M. Leja, K. Unterkofler, C. Jaeschke, R. Skapars, E. Gasenko, I. Polaka, E. Vasiljevs, G. Shani, J. Mitrovics, C.A. Mayhew, H. Haick, Non-contact breath sampling for sensor-based breath analysis, J. Breath Res. 13 (2019) 036001, https://doi.org/10.1088/1752-7163/ab0b8d.
[2] F. Qu, Y. Yuan, M. Yang, Programmed synthesis of Sn3N4 nanoparticles via a soft chemistry approach with urea: application for ethanol vapor sensing, Chem. Mater. 29 (2017) 969–974, https://doi.org/10.1021/acs.chemmater.6b03435.
[3] Y. Zhao, B. Dong, K.D. Benkstein, L. Chen, K.L. Steffens, S. Semancik, Deep learning image analysis of nanoplasmonic sensors: toward medical breath monitoring, ACS Appl. Mater. Interfaces 14 (2022) 54411–54422, https://doi.org/10.1021/acsami.2c11153.
[4] S. Mojumder, T. Das, M. Mukherjee, D. Saha, A. Datta, M. Pal, Development of highly sensitive and selective trace acetone sensor using perovskite yttrium ferrite: mechanism, kinetics and phase dependence study, Chem. Eng. J. 477 (2023) 146855, https://doi.org/10.1016/j.cej.2023.146855.
[5] V. Ruzsányi, M.P. Kalapos, Breath acetone as a potential marker in clinical practice, J. Breath Res. 11 (2017) 024002, https://doi.org/10.1088/1752-7163/aa66d3.
[6] Z. Wang, C. Wang, Is breath acetone a biomarker of diabetes? A historical review on breath acetone measurements, J. Breath Res. 7 (2013) 037109, https://doi.org/10.1088/1752-7155/7/3/037109.
[7] S.I. Hwang, H.-Y. Chen, C. Fenk, M.A. Rothfuss, K.N. Bocan, N.G. Franconi, G. J. Morgan, D.L. White, S.C. Burkert, J.E. Ellis, M.L. Vinay, D.A. Rometo, D. N. Finegold, E. Sejdic, S.K. Cho, A. Star, Breath acetone sensing based on single-walled carbon nanotube–titanium dioxide hybrids enabled by a custom-built dehumidifier, ACS Sensors 6 (2021) 871–880, https://doi.org/10.1021/acssensors.0c01973.
[8] X. Liu, X. Tian, X. Jiang, L. Jiang, P. Hou, S. Zhang, X. Sun, H. Yang, R. Cao, X. Xu, Facile preparation of hierarchical Sb-doped In2O3 microstructures for acetone

detection, Sens. Actuators B Chem., 270 (2018) 304–311, https://doi.org/10.1016/j.snb.2018.05.046.
[9] A. Shanmugasundaram, K. Munirathinam, D.-W. Lee, SnO2 nanostructure-based acetone sensors for breath analysis, Micro Nano Syst. Lett. 12 (2024) 3, https://doi.org/10.1186/s40486-023-00196-5.
[10] Y. Wang, C. Liu, Z. Wang, Z. Song, X. Zhou, N. Han, Y. Chen, Sputtered SnO2:NiO thin films on self-assembled au nanoparticle arrays for MEMS compatible NO2 gas, Sens. Actuators B Chem., 278 (2019) 28–38, https://doi.org/10.1016/j.snb.2018.09.074.
[11] V.V. Kondalkar, L.T. Duy, H. Seo, K. Lee, Nanohybrids of Pt-functionalized Al2O3/ZnO core−shell nanorods for high-performance MEMS-based acetylene gas sensor, ACS Appl. Mater. Interfaces 11 (2019) 25891–25900, https://doi.org/10.1021/acsami.9b06338.
[12] A. Shanmugasundaram, D.-S. Kim, N.D. Chinh, J. Park, Y.-J. Jeong, J. Piao, D. Kim, D.W. Lee, N-/S- dual doped C@ZnO: an excellent material for highly selective and responsive NO2 sensing at ambient temperatures, Chem. Eng. J. 421 (2021) 127740, https://doi.org/10.1016/j.cej.2020.127740.
[13] A. Shanmugasundaram, P. Basak, L. Satyanarayana, S.V. Manorama, Hierarchical SnO/SnO2 nanocomposites: formation of in situ p–n junctions and enhanced H2 sensing, Sens. Actuators B: Chem., 185 (2013) 265–273, https://doi.org/10.1016/j.snb.2013.04.097.
[14] A. Shanmugasundaram, D.W. Lee, SnO2/rGO nanocomposite for the detection of biomarkers of lung cancer, Micro Nano Syst. Lett. 10 (2022) 13, https://doi.org/10.1186/s40486-022-00154-7.
[15] C. Li, P.G. Choi, Y. Masuda, Large-lateral-area SnO2 nanosheets with a loose structure for high-performance acetone sensor at the ppt level, J. Hazard. Mater., 455 (2023) 131592, https://doi.org/10.1016/j.jhazmat.2023.131592.
[16] X. Li, Y. Liu, S. Li, J. Huang, Y. Wu, D. Yu, The sensing properties of single Y-doped SnO2 nanobelt device to acetone, Nanoscale Res. Lett. 11 (2016) 1–8, https://doi.org/10.1186/s11671-016-1685-1.
[17] T.T. Wang, S.Y. Ma, L. Cheng, X.H. Jiang, M. Zhang, W.Q. Li, W.X. Jin, Facile fabrication of multishelled SnO2 hollow microspheres for gas sensing application, Mater. Lett., 164 (2016) 56–59, https://doi.org/10.1016/j.matlet.2015.10.118.
[18] W.Q. Li, S.Y. Ma, J. Luo, Y.Z. Mao, L. Cheng, D.J. Gengzang, X.L. Xu, S.H. Yan, Synthesis of hollow SnO2 nanobelts and their application in acetone sensor, Mater. Lett., 132 (2014) 338–341, https://doi.org/10.1016/j.matlet.2014.06.112.
[19] Q. Wang, N. Yao, D. An, Y. Li, Y. Zou, X. Lian, X. Tong, Enhanced gas sensing properties of hierarchical SnO2 nanoflower assembled from nanorods via a one-pot template-free hydrothermal method, Ceram. Int. 42 (2016) 15889–15896, https://doi.org/10.1016/j.ceramint.2016.07.062.
[20] T. Wang, L. Cheng, Hollow hierarchical TiO2-SnO2-TiO2 composite nanofibers with increased active-sites and charge transfer for enhanced acetone sensing performance, Sens. Actuators B Chem., 334 (2021) 129644, https://doi.org/10.1016/j.snb.2021.129644.
[21] C. Li, K. Kim, T. Fuchigami, T. Asaka, K.I. Kakimoto, Y. Masuda, Acetone gas sensor based on Nb2O5@SnO2 hybrid structure with high selectivity and ppt-level sensitivity, Sens. Actuators B Chem., 393 (2023) 134144, https://doi.org/10.1016/j.snb.2023.134144.
[22] V.K. Tomer, K. Singh, H. Kaur, M. Shorie, P. Sabherwal, Rapid acetone detection using indium loaded WO3/SnO2 nanohybrid sensor, Sens. Actuators B Chem., 253 (2017) 703–713, https://doi.org/10.1016/j.snb.2017.06.179.
[23] L. Cheng, S.Y. Ma, T.T. Wang, J. Luo, Synthesis and enhanced acetone sensing properties of 3D porous flower-like SnO nanostructures, Mater. Lett., 143 (2015) 84–87, https://doi.org/10.1016/j.matlet.2014.12.062.
[24] T. Zhou, S. Cao, N. Sui, J. Tu, T. Zhang, Ultra-sensitive detection of acetone based on Zn-Fe spinel type ferrites, Sens. Actuators B Chem., 344 (2021) 130152, https://doi.org/10.1016/j.snb.2021.130152.
[25] X. Ji, J. Chang, Z. Deng, C. Shen, M. Li, S. Wang, L. You, M. Kumar, X. Fang, G. Meng, Boosting acetone response of p-type Co_3O_4 sensor via Sn and Ni co-doping for diabetes diagnosis, Sens. Actuators B Chem., 410 (2024) 135705, https://doi.org/10.1016/j.snb.2024.135705.
[26] L. He, J. Hu, Q. Yuan, Z. Xia, L. Jin, H. Gao, L. Fan, X. Chu, F. Meng, Synthesis of porous ZnFe2O4/SnO2 core-shell spheres for high-performance acetone gas sensing, Sens. Actuators B: Chem., 378 (2023) 133123, https://doi.org/10.1016/j.snb.2022.133123.
[27] W. Wang, J. Xian, J. Li, M. Yu, Q. Duan, C.M. Leung, M. Zeng, X. Gao, Construction of Co3O4/SnO2 yolk-shell nanofibers for acetone gas detection, Sens. Actuators B: Chem., 398 (2024) 134724, https://doi.org/10.1016/j.snb.2023.134724.
[28] B.-Y. Song, J. Huang, Z.-Q. Cui, X.-F. Zhang, Z.-P. Deng, Y.-M. Xu, L.-H. Huo, S. Gao, Temperature-controlled dual-selectivity nitric oxide/acetone sensor constructed from mesoporous SnO2 tubes doped by biomass-derived graphitic carbon, Appl. Surf. Sci. 623 (2023) 157009, https://doi.org/10.1016/j.apsusc.2023.157009.
[29] J. Hu, X. Xiong, W. Guan, C. Tan, Hollow mesoporous SnO2/Zn2SnO4 heterojunction and RGO decoration for high-performance detection of acetone, ACS Appl. Mater. Interfaces 14 (2022) 55249–55263, https://doi.org/10.1021/acsami.2c18255.
[30] F. Li, J. Jing, J. Li, S. Li, S. Ye, X. Song, Z. Zhan, Y. Zhang, Fabrication of ZnO-SnO2 heterojunction inverse opal photonic balls for chemiresistive acetone sensing, Sens. Actuators B Chem., 400 (2024) 134887, https://doi.org/10.1016/j.snb.2023.134887.
[31] D.-H. Kim, J.-S. Jang, W.-T. Koo, S.-J. Choi, S.-J. Kim, I.-D. Kim, Hierarchically interconnected porosity control of catalyst-loaded WO3 nanofiber scaffold: superior acetone sensing layers for exhaled breath analysis, Sens. Actuators B Chem., 259 (2018) 616–625, https://doi.org/10.1016/j.snb.2017.12.051.
[32] Y.J. Jeong, W.-T. Koo, J.-S. Jang, D.-H. Kim, M.-H. Kim, I.-D. Kim, Nanoscale PtO2 catalysts-loaded SnO2 multichannel nanofibers toward highly sensitive acetone sensor, ACS Appl. Mater. Interfaces 10 (2018) 2016–2025, https://doi.org/10.1021/acsami.7b16258.
[33] S.-J. Choi, B.-H. Jang, S.-J. Lee, B.K. Min, A. Rothschild, I.-D. Kim, Selective detection of acetone and hydrogen sulfide for the diagnosis of diabetes and halitosis using SnO2 nanofibers functionalized with reduced graphene oxide nanosheets, ACS Appl. Mater. Interfaces 6 (2014) 2588–2597, https://doi.org/10.1021/am405088q.
[34] B. Jiang, T. Zhou, L. Zhang, J. Yang, W. Han, Y. Sun, F. Liu, P. Sun, H. Zhang, G. Lu, Separated detection of ethanol and acetone based on SnO2-ZnO gas sensor with improved humidity tolerance, Sens. Actuators B Chem., 393 (2023) 134257, https://doi.org/10.1016/j.snb.2023.134257.
[35] S. Salehi, E. Nikan, A.A. Khodadadi, Y. Mortazavi, Highly sensitive carbon nanotubes–SnO2 nanocomposite sensor for acetone detection in diabetes mellitus breath, Sens. Actuators B Chem., 205 (2014) 261–267, https://doi.org/10.1016/j.snb.2014.08.082.
[36] S. Jin, D. Wu, W. Song, H. Hao, W. Gao, S. Yan, Superior acetone sensor based on hetero-interface of SnSe2/SnO2 quasi core shell nanoparticles for previewing diabetes, J. Colloid Interface Sci. 621 (2022) 119–130, https://doi.org/10.1016/j.jcis.2022.04.057.
[37] P.M. Bulemo, D.H. Kim, I.D. Kim, Controlled synthesis of electrospun hollow Pt-loaded SnO2 microbelts for acetone sensing, Sens. Actuators B Chem., 344 (2021) 130208, https://doi.org/10.1016/j.snb.2021.130208.
[38] L. Guo, Z. Shen, C. Ma (x2), J. Wang, T. Yuan, Gas sensor based on MOFs-derived Au-loaded SnO2 nanosheets for enhanced acetone detection, J. Alloy. Compd. 906 (2022) 164375, https://doi.org/10.1016/j.jallcom.2022.164375.
[39] G. Li, Z. Cheng, Q. Xiang, L. Yan, X. Wang, J. Xu, Bimetal PdAu decorated SnO2 nanosheets based gas sensor with temperature-dependent dual selectivity for detecting formaldehyde and acetone, Sens. Actuators B Chem. 283 (2019) 590–601, https://doi.org/10.1016/j.snb.2018.09.117.
[40] Y. Li, L. Qiao, D. Yan, L. Wang, Y. Zeng, H. Yang, Preparation of Au-sensitized 3D hollow SnO2 microspheres with an enhanced sensing performance, J. Alloy. Compd. 586 (2014) 399–403, https://doi.org/10.1016/j.jallcom.2013.09.147.
[41] X. Kou, N. Xie, F. Chen, T. Wang, L. Guo, C. Wang, Q. Wang, J. Ma, Y. Sun, H. Zhang, G. Lu, Superior acetone gas sensor based on electrospun SnO2 nanofibers by Rh doping, Sens. Actuators B Chem., 256 (2018) 861–869, https://doi.org/10.1016/j.snb.2017.10.011.
[42] M.S. Jo, et al., Coral-like yolk-shell-structured nickel oxide/carbon composite microspheres for high-performance Li-ion storage anodes, Nano-Micro Letters 11 (2019) 18, https://doi.org/10.1007/s40820-018-0234-0.
[43] W.S. Hummers Jr., R.E. Offeman, Preparation of graphitic oxide, J. Am. Chem. Soc. 80 (1958) 1339, https://doi.org/10.1021/ja01539a017.
[44] A. Shanmugasundaram, S.V. Manorama, D.-S. Kim, Y.-J. Jeong, D.W. Lee, Toward Point-of-Care chronic disease Management: Biomarker detection in exhaled breath using an E-Nose sensor based on rGO/SnO2 superstructures, Chem. Eng. J. 448 (2022) 137736, https://doi.org/10.1016/j.cej.2022.137736.
[45] D.-F. Zhang, L.-D. Sun, J.-L. Yin, C.-H. Yan, Low-temperature fabrication of highly crystalline SnO2 nanorods, Adv. Mater. 15 (2003) 913–917, https://doi.org/10.1002/adma.200304899.
[46] T. Akita, T. Hiroki, S. Tanaka, T. Kojima, M. Kohyama, A. Iwase, F. Hori, Analytical TEM observation of Au–Pd nanoparticles prepared by sonochemical method, Catal. Today 131 (2008) 90–97, https://doi.org/10.1016/j.cattod.2007.10.033.
[47] D. Wang, X. Guo, G. Zhang, Y. Liu, S. Liu, Z. Zhang, Y. Chai, Y. Chen, J. Zhang, B. Sun, SnO2 electron transport layer modified by F/N-doped graphdiyne and in situ XRD and in situ XAFS exploration on its effect on perovskite active layer, Nano Today 50 (2023) 101852, https://doi.org/10.1016/j.nantod.2023.101852.
[48] P. Murugesh, M. Ganesan, P.S. Udaiyar, H.S. Krishnan, A. Jayaram, N. Mani, Mesoporous Co3O4/SnO2 nanostructure-based heterojunctions for NO2 sensors, ACS Appl. Nano Mater. 6 (2023) 17433–17444, https://doi.org/10.1021/acsanm.3c02327.
[49] K. Komal, G. Gupta, M. Singh, B. Singh, Improved resistive switching of RGO and SnO2 based resistive memory device for non-volatile memory application, J. Alloy. Compd. 923 (2022) 166196, https://doi.org/10.1016/j.jallcom.2022.166196.
[50] H. Bai, H. Guo, C. Feng, J. Wang, B. Liu, Z. Xie, F. Guo, D. Chen, R. Zhang, Y. Zheng, A room-temperature chemiresistive NO2 sensor based on one-step synthesized SnO2 nanospheres functionalized with Pd nanoparticles and rGO nanosheets, Appl. Surf. Sci. 575 (2022) 151698, https://doi.org/10.1016/j.apsusc.2021.151698.
[51] A. Shanmugasundaram, N.D. Chinh, Y.-J. Jeong, T.F. Hou, D.-S. Kim, D. Kim, Y.-B. Kim, D.-W. Lee, Hierarchical nanohybrids of B-and N-codoped graphene/mesoporous NiO nanodisks: an exciting new material for selective sensing of H2S at near ambient temperature, J. Mater. Chem. A 7 (2019) 9263–9278, https://doi.org/10.1039/C9TA00755E.
[52] A. Shanmugasundaram, V. Gundimeda, T. Hou, D.W. Lee, Realizing synergy between In2O3 nanocubes and nitrogen-doped reduced graphene oxide: an excellent nanocomposite for the selective and sensitive detection of CO at ambient temperatures, ACS Appl. Mater. Interfaces 9 (2017) 31728–31740, https://doi.org/10.1021/acsami.7b06253.
[53] Q. Li, Q. Wei, L. Xie, C. Chen, C. Lu, F.Y. Su, P. Zhou, Layered NiO/reduced graphene oxide composites by heterogeneous assembly with enhanced performance as high-performance asymmetric supercapacitor cathode, RSC Adv. 6 (2016) 46548–46557, https://doi.org/10.1039/C6RA04998B.
[54] A.S. Khder, H.M. Altass, R.S. Jassas, M.M. Al-Rooqi, M.A. Khder, M. Morad, A. Gebreil, Z. Moussa, S.A. Ahmed, Room-temperature CO oxidation over Au–Pd

monometallic and bimetallic nanoparticle-supported MgO, ACS Appl. Nano Mater. 6 (2023) 4243–4252, https://doi.org/10.1021/acsanm.2c05326.
[55] K. Jabłczynska, A. Gogos, C.M.P. Kubsch, S.E. Pratsinis, Embedding Pd into SnO2 drastically enhances gas sensing, Nanoscale Adv. 6 (2024) 1259–1268, https://doi.org/10.1039/D3NA00558E.
[56] B.K. Mutuma, S. Eom, T. Goto, H. Park, Y. Kondo, S.H. Cho, C. Cho, T. Sekino, Morphological features and electrical properties of hollow SnO2 for room temperature CO sensing, Ceram. Int. 49 (2023) 34976–34984, https://doi.org/10.1016/j.ceramint.2023.08.171.
[57] W. Wang, Y. Chen, L. Lei, Z. Wan, S. Tang, Q. Zhong, H. Wang, H. Fan, Heterojunctions comprised of graphitic carbon nitride nanosheets and SnO2 nanoparticles with exposed 221 crystal facets for photocatalytic hydrogen evolution, ACS Appl. Nano Mater. (2023), https://doi.org/10.1021/acsanm.3c03501.
[58] L. He, J. Hu, Q. Yuan, Z. Xia, L. Jin, H. Gao, L. Fan, X. Chu, F. Meng, Synthesis of porous ZnFe2O4/SnO2 core-shell spheres for high- performance acetone gas sensing, Sens. Actuators B Chem., 378 (2023) 133123, https://doi.org/10.1016/j.snb.2022.133123.
[59] M. Liu, P. Song, Z. Yang, Q. Wang, Hierarchical assembly of SnO2 nanorod on spindle-like α-Fe2O3 for enhanced acetone gas-sensing performance, Ceram. Int. 47 (2021) 12181–12188, https://doi.org/10.1016/j.ceramint.2021.01.065.
[60] J. Lu, Y. Xie, F. Luo, H. Fu, X. Huang, Y. Liu, H. Liu, Heterostructures of mesoporous hollow Zn2SnO4/SnO2 microboxes for high-performance acetone sensors, J. Alloy. Compd. 844 (2020) 155788, https://doi.org/10.1016/j.jallcom.2020.155788.
[61] X. Xu, Y. Chen, G. Zhang, S. Ma, Y. Lu, H. Bian, Q. Chen, Highly sensitive VOCs-acetone sensor based on Ag-decorated SnO2 hollow nanofibers, J. Alloy. Compd. 703 (2017) 572–579, https://doi.org/10.1016/j.jallc om.2017.01.348.
[62] Z. Jiang, R. Zhao, B. Sun, G. Nie, H. Ji, J. Lei, C. Wang, Highly sensitive acetone sensor based on Eu-doped SnO2 electrospun nanofibers, Ceram. Int. 42 (2016) 15881–15888, https://doi.org/10.1016/j.ceramint.2016.07.060.
[63] Z. Jiang, C. Wang, Z. Yang, L. Zhang, J. Jin, X. Guo, L. Zhong, Z. Duan, H. Li, Electrospun Eu2O3/Au/SnO2 ternary nanofibers with synergistIcally enhanced acetone sensing properties, Mater. Lett., 304 (2021) 130729, https://doi.org/10.1016/j.matlet.2021.130729.
[64] X. Kou, F. Meng, K. Chen, T. Wang, P. Sun, F. Liu, X. Yan, Y. Sun, F. Liu, K. Shimanoe, G. Lu, High-performance acetone gas sensor based on Ru-doped SnO2 nanofibers, Sen. Actuators B Chem., 320 (2020) 128292, https://doi.org/10.1016/j.snb.2020.128292.
[65] D. Lian, B. Shi, R. Dai, X. Jia, X. Wu, Synthesis and enhanced acetone gas-sensing performance of ZnSnO3/ SnO2 hollow urchin nanostructures, J. Nanopart. Res., 19 (2017) 1–8, https://doi.org/10.1007/s11051-017-4094-1.
[66] X. Lian, Y. Li, X. Tong, Y. Zou, X. Liu, D. An, Q. Wang, Synthesis of Ce- doped SnO2 nanoparticles and their acetone gas sensing properties, Appl. Surf. Sci. 407 (2017) 447–455, https://doi.org/10.1016/j.apsusc.2017.02.228.
[67] P. Cheng, L. Lv, Y. Wang, B. Zhang, Y. Zhang, Y. Zhang, Z. Lei, L. Xu, SnO2/ZnSnO3 double-shelled hollow microspheres based high-perfor- mance acetone gas sensor, Sen. Actuators B Chem., 332 (2021) 129212, https://doi.org/10.1016/j.snb.2020.129212.
[68] F. Li, X. Gao, R. Wang, T. Zhang, G. Lu, Study on TiO2- SnO2 core-shell heterostructure nanofibers with different work function and its application in gas sensor, Sen. Actuators B Chem., 248 (2017) 812–819, https://doi.org/10.1016/j.snb.2016.12.009.
[69] W.T. Koo, J.S. Jang, S.J. Choi, H.J. Cho, I.D. Kim, Metal–organic frame- work templated catalysts: dual sensitization of PdO–ZnO composite on hollow SnO2 nanotubes for selective acetone sensors, ACS Appl. Mater. Inter., 9 (2017) 18069–18077, https://doi.org/10.1021/acsami.7b04657.
[70] J. Shin, S.J. Choi, I. Lee, D.Y. Youn, C.O. Park, J.H. Lee, H.L. Tuller, I.D. Kim, Thin-wall assembled SnO2 fibers functionalized by catalytic Pt nano- particles and their superior exhaled-breath-sensing properties for the diagnosis of diabetes, Adv. Funct. Mater., 23 (2013) 2357–2367, https://doi.org/10.1002/adfm.201202729.